Numerical modeling and experimental validation of uniform microchamber filling in centrifugal microfluidics†

Jonathan Siegrist,*[a] Mary Amasia,[a] Navdeep Singh,[b] Debjyoti Banerjee[b] and Marc Madou[a]

Received 1st September 2009, Accepted 4th December 2009
First published as an Advance Article on the web 12th January 2010
DOI: 10.1039/b917880e

In this paper, a comprehensive approach to numerical and experimental analysis of microchamber filling in centrifugal microfluidics is presented. In the development of micro total analysis systems, it is often necessary to achieve complete, uniform filling of relatively large microchambers, such as those needed for nucleic acid amplification or detection. With centrifugal devices, these large microchambers must often be orientated perpendicularly to the direction of centrifugal force and are usually bounded by materials with varying surface properties. The resulting fluidic flow in such systems can be complex and is not well characterized. To gain further insight into complex fluidic behavior on centrifugal microfluidic platforms, numerical modeling using the Volume of Fluids method is performed to simulate microchamber filling in a centrifugal microfluidic device with integrated sample preparation, amplification, and detection capabilities. Parametric analyses are performed using numerical models to predict microchamber filling behavior for a range of pressure conditions. High-speed flow visualization techniques are used to track the liquid meniscus during filling of the microchambers, and comparison to the numerical predictions for experimental validation is achieved by analyzing the liquid volume fraction as a function of the non-dimensional temporal profile during filling. When channel filling profiles are compared, the numerical model predictions utilizing static conditions are in strong agreement with the experimental data. When dynamic modeling conditions are used, the numerical predictions are extremely accurate as compared to the experimental data.

1. Introduction

A recent trend in the integration of molecular diagnostics and microfluidics is towards the development of integrated, miniaturized diagnostic devices, or micro total analysis systems (μTAS). Motivation behind the creation of such devices stems primarily from a number of inherent advantages including lower space requirements, reduced reagent and sample consumption, improved analysis times, disposability, automation, and improved assay performance.[1,2] The biggest challenge in the development of μTAS devices is to design a disposable device that combines multiple steps,[3] and thus much R&D effort in both academia and industry has been put towards crucial engineering aspects of these systems: device prototyping and manufacturing,[4–8] physical and chemical characterization of fluid flow and device material,[9–11] and various on-chip hardware systems.[12–14] In particular, centrifugal microfluidic systems have been a focus for almost 40 years, and hold many advantages for integration of multiple, complex biological analysis steps.[1]

1.1 Compact disc-like centrifugal microfluidic platforms

The compact disc (CD)-like centrifugal microfluidic platform holds many advantages due to its unique pumping and valving mechanisms.[15–17] Centrifugal pumping is dependent in part on rotation frequency and radial distance from the CD center, but is relatively insensitive to physicochemical properties such as pH, ionic strength, and chemical composition of the fluid being pumped; this is in stark contrast to the AC and DC electrokinetic means of pumping.[16] Today's more common pressure-driven syringe and peristaltic pumping methods provide good control at larger flow rates, but can be unwieldy when trying to miniaturize and/or process in parallel, making implementation into small, multiplexed platforms difficult.[1] Since the types and the amounts of fluids one can pump on a centrifugal platform spans a greater dynamic range than for electrokinetic, acoustic, or peristaltic pumps, the centrifugal approach is more amenable to sample preparation tasks where fluidic properties can vary significantly from sample to sample.

Fluidic valving on CD platforms is commonly accomplished using simple, passive surface tension valves in which capillary forces pin fluids at channel enlargements or restrictions, depending on the hydrophilicity of the channel material.[15,16] The fluid is held at the valve until rotationally-induced pressure is sufficient to overcome the capillary pressure (at the so-called

[a]*University of California, Irvine, Irvine, CA, 92697, USA. E-mail: jsiegris@uci.edu*
[b]*Texas A&M University, College Station, TX, 77843, USA*

† Electronic supplementary information (ESI) available: Movie A – strobe-image video of the experimental PCR microchamber filling – note one frame is collected per CD rotation; Movie B – movie of numerical simulation from condition D, showing fluid flow; Movie C – movie of numerical simulation from condition D, showing fluid velocity; Movie D – movie of numerical simulation from condition H, showing fluid flow; Fig. A_ESI – Numerical grids used to discretize the computational domain. (A) Overview of grid distribution in the PCR microchamber, (B) expanded view showing the local grid distribution at the inlet of the microchamber, and (C) expanded view showing the local grid distribution at the outlet of the microchamber. See DOI: 10.1039/b917880e

burst frequency). In addition, a large range of microfluidic functions including valving, decanting, calibration, mixing, metering, sample splitting, and separation have been implemented on centrifugal systems. Within this platform, analytical measurements may be electrochemical, fluorescent, or absorption-based, and informatics can be embedded on the same disc to provide test-specific information.[15–18]

A majority of the microfluidic devices for clinical diagnostic applications have been limited to single molecular diagnostic steps due to the complexity of integrating various microfluidic components into a single, small, disposable unit, without emphasis on the necessary sample preparation steps (*e.g.*, lysis, purification, concentration).[19] Compared to other microfluidic technologies, a centrifuge-based system is well suited for the integration of various functions, including sample preparation.[20,21] Through the exploitation of the centrifugal and Coriolis forces in combination with the capillary force, microfluidic functions and biological analysis steps can be integrated onto a single CD device.

1.2 Numerical modeling of centrifugal microfluidics

With the integration of complex fluidic steps comes the need for a better understanding of the physical behavior in such advanced systems. Characterization of centrifugal platforms in particular can be quite complex, as various forces and pseudo forces that result from the rotating reference frame must be taken into account. Several reports in the literature describe the development of numerical models and experimental validation of the predictions from these models for individual components of centrifugal microfluidic platforms for microfluidic characterization.[22–26] Earlier efforts by Banerjee *et al.*[22] were successful in developing models of individual components for CD platforms, such as actuation of the capillary burst valve[22] using the Volume of Fluids (VOF) method.[27] However, a fundamental aspect of centrifugal microfluidic platforms, filling and emptying of chambers and channels in complex systems, has not been thoroughly investigated.

1.3 Uniform microchamber filling

A majority of CD platform applications involve molecular diagnostic technologies and methods, such as those for nucleic acid (NA) analysis. At the core of NA analysis are steps such as enzymatic-based NA amplification (*e.g.*, Polymerase Chain Reaction, or PCR) and NA detection *via* microarrays. Conventional microfluidic PCR requires repeated thermocycling of analyte NA in a microchamber, and the thermal homogeneity of the PCR volume is a crucial factor in the run-time, efficiency, specificity, and limit-of-detection of the amplification reaction(s). Hence, the uniform filling of PCR microchambers (*viz.*, with a prepared biological sample) is a critical initial step for successful implementation of PCR.[28–30] In the case of DNA microarray chambers, uniform filling (*viz.*, with a PCR product) is essential for efficient DNA hybridization. There are numerous other situations in which uniform, bubble-free chamber filling on CD platforms is crucial to both device and assay performance. However, no comprehensive analysis (combining numerical modeling with experimental validation) has yet been reported for uniform filling of microfluidic chambers on centrifugal platforms with complex surface interactions.[31–33]

1.4 PCR microchamber design and justification

A typical, integrated device for NA diagnostics consists of a sample preparation step, an amplification step, and a detection step. Here, a CD platform is presented that combines all three steps towards a CD-based μTAS system for DNA detection of bacteria in respiratory samples. Briefly, the CD consists of sample preparation *via* mechanical cell lysis, followed by centrifugal clarification of the sample. Madou *et al.* have previously shown proof-of-concept for this CD-based mechanism.[30] The prepared sample is then sent to a PCR channel/chamber for simultaneous NA amplification and fluorescence detection *via* real-time PCR (Fig. 1). As previously published by Madou *et al.*, rapid and efficient PCR thermocycling in a microchamber is achieved by contact with Peltier thermoelectric devices; thermoelectrics are also used to freeze a small amount of liquid in the PCR microchamber inlets and outlets to serve as an ice-valve (that hold both liquid and vapor) during thermocycling.[29]

PCR microchambers must remain thin to facilitate rapid thermocycling,[29] but need a relatively large surface area to contain the appropriate amount of liquid. A typical, clinically-relevant PCR reaction volume is on the order of 15–50 μL. If this volume is contained within a microchamber 200 μm thick, the surface area of the chamber can be large, ranging from 75–250 mm^2. On microfluidic centrifugal platforms, long, wide chambers such as these can be difficult to fill uniformly, due to the non-uniformities of the pressure gradients present in chambers/channels that span large radial distances. Eqn (1)

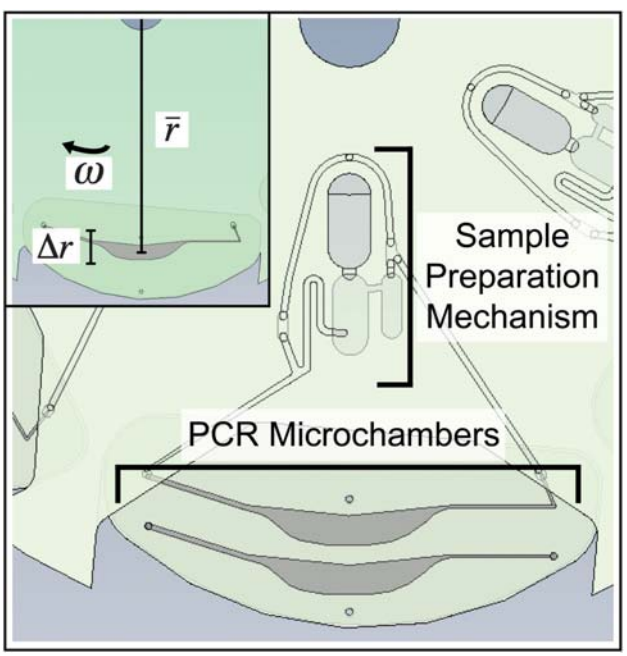

Fig. 1 Schematic showing the sample preparation and PCR microchamber features. One PCR microchamber is integrated with sample preparation fluidics, while the other serves as an assay reference; Inset: Schematic showing the small change in radial distances obtained when microchambers are oriented perpendicular to the centrifugal force.

describes the pressure at the meniscus of a radially-oriented fluid plug subjected to a centrifugal force:

$$P_m = \rho\omega^2\bar{r}\Delta r \quad (1)$$

where ρ is density of the fluid, ω is the angular velocity of the CD (*i.e.*, spin speed), $\bar{r}$ is the average distance from the liquid element to the center of the CD, and Δr is the radial span of the liquid sample (Fig. 1, inset).[16] In chambers with large Δr values, non-uniformities such as air bubbles can develop as filling occurs across the resulting large pressure difference. To reduce these effects, large, long chambers should be oriented perpendicular to the centrifugal force, such that pressure differences during filling are minimized (by minimizing Δr), resulting in uniform filling. Moreover, long, wide chambers/channels can occupy crucial radial real estate on CD platforms. In order to free up space and allow integration with other features, they must be oriented perpendicular to the centrifugal force.

Fluidic behavior in systems such as these is subject to the complex forces and surface interactions present. In a DNA microarray device, the substrate can be a hydrophilic glass slide, while the channel itself can consist of a hydrophobic silicone material.[29] In a PCR chamber, the roof may be surface-treated hydrophilic plastic, while the chamber bottom may be a hydrophobic metal foil (to facilitate heat transfer).[29] Coriolis, capillary, and centrifugal forces are all present in such systems and influence microchamber filling. Microchamber filling in such centrifugal systems is not well understood, but is crucial to efficient microfluidic and biological performance.

This study reports on the development of numerical models for microchamber filling in a novel centrifugal microfluidic platform with integrated sample preparation, amplification, and detection capabilities. Numerical models are developed using the VOF method,[27] and predictions from the numerical models are compared with experimental results. This results in combined numerical and experimental analyses of microchamber filling in centrifugal microfluidics, with models that can be generalized for filling and emptying on other microfluidic platforms.

2. Experimental materials and methods

2.1 CD fabrication

The CDs designed and tested here consist of multi-layer structures made of inexpensive polycarbonate plastic (McMaster-Carr, CA, USA), pressure-sensitive adhesives (PSA) (FLEXcon, MA, USA, FLEXmount® DFM 200 Clear V-95 150 Poly H-9 V-95 400 Poly H-95 4), and adhesive-backed foil films (Excel Scientific, CA, USA-AlumaSeal II foil). Using a relatively simple CNC machine (T-Tech, GA, USA-QuickCircuit 5000), channel widths down to 1 mm can be machined into stock polycarbonate. A computer-controlled cutter-plotter (Graphtec, Japan-Graphtec CE-2000) is used to cut channel widths as narrow as 200 μm in thinner materials such as 100 μm-thick PSA or adhesive foil films. Once the appropriate pieces have been designed and machined, they are aligned centrally and radially, and laminated together using the PSA layers. The microfluidic CD device presented consists of 7 layers: (1) top polycarbonate CD with CNC-machined sample loading, sample removal, and air venting holes (sealed using a thin adhesive film during operation), (2) pressure-sensitive adhesive with channel features cut using a plotter, (3) middle polycarb. CD with CNC chamber features, (4) and (5) pressure-sensitive adhesive layers with PCR microchamber features cut using a plotter, doubled-up to obtain a larger thickness, (6) solid bottom polycarb. CD, and (7) thin adhesive foil films cut using a plotter to seal off the PCR microchambers (Fig. 2). The fabrication process ends with running the CDs through an industrial press to ensure excellent adhesion and sealing between all layers. It should be noted that the PCR microchamber geometries were designed specifically for the centrifugal platform, with the contours of the upper and lower walls, including the inlet channel, following the CD radii at those locations (Fig. 1).

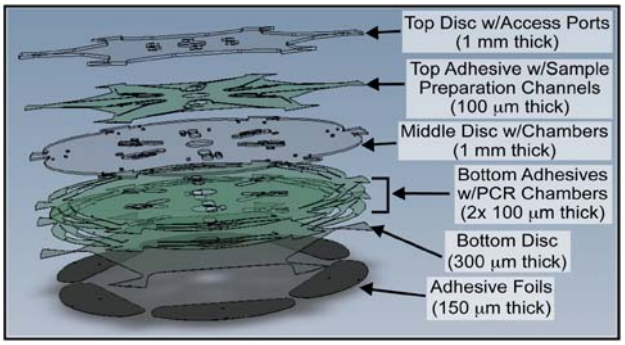

Fig. 2 Schematic showing the layers involved in CD fabrication and assembly. The PCR microchambers consist of holes in the bottom adhesives, with solid plastic (middle disc) as the roof and adhesive foil as the floor.

The CD devices tested rely on O_2 plasma treatment to render the polycarbonate surfaces hydrophilic, essential to the function of the siphon component of the sample preparation.[17,30] A Technics 500II Asher was used at an O_2 pressure of 200 mTorr with 200 W of power for 2.5 mins for hydrophilization of the un-assembled polycarbonate CD layers.

2.2 CD testing and image acquisition

Experimental testing of the μTAS CDs was carried out by strobe-imaging of the CD during operation. Approximately 30–60 μL of DI water containing < 1% v/v of a contrast agent (McCormick, MD, US-Neon food dye) was placed inside the CD, and the CD placed on a spin-stand equipped with a rotational motor (Pacific Scientific Servo Motor) and an amplifier/controller (PAC SCI Programmable Servo Drive) which enables various rotational profiles and precise positioning. The servo drive uses a graphical user interface program, ToolPAC, to easily configure and program the motor for specific applications. The CD to be tested is placed on an aluminium chuck coupled to the motor shaft and locked in place.

The imaging system allows viewing of a sequence of color images of the area of interest on the CD in real time (while it is rotating) and storage of the captured frames on a computer. The imaging system is composed of: a camera (Basler A301bc, 640 × 480 pixels, 80 fps max., 10× zoom lens mounted), a strobe light (PerkinElmer MVS-4200, 6 μs duration), and a retro-reflective fiber-optic sensor (Banner D10 Expert Fiber-Optic Sensor). The strobe light, with a 100 Hz maximum repetition

frequency, is employed to reduce blurry images of the fast moving CDs. In order to generate synchronized signals, a reflective marker (~2 mm × 2 mm) is placed on the surface of the CD and aligned with the fiber-optic sensor. When the sensor detects the marker, a signal pulse is sent to the video capture board, triggering the camera and strobe light to acquire one image frame per CD revolution.

Using this system, the test fluid was centrifugally driven through the sample preparation fluidic elements. After siphon priming at a lower CD spin speed, PCR channel/chamber filling was performed by increasing the spin speed of the CD to 2000 revolutions-per-minute (RPM) and at an average acceleration of 500 RPM/s. Images were acquired during PCR microchamber filling, and later compared to the developed numerical models.

2.3 Contact angle measurements

Contact angle measurements of the CD materials were performed to support development of the numerical models. This included measurements of native and O_2-plasma treated polycarbonate in addition to exposed adhesive (*viz.*, PSA). Contact angle measurements were obtained using a goniometer (Kruss GmbH, Germany-Kruss DSA) at the Center for Materials Characterization at the Texas Transportation Institute. The results from these measurements are summarized in Table 1.

Since plasma treatment of polycarbonate does not provide a particularly stable form of surface treatment, it is expected that the polycarbonate surfaces age with time. Therefore, the contact angle for the treated polycarbonate substrates is expected to vary between ~40°–80°;[34] the treated polycarbonate substrate can thus be considered to behave as a mildly hydrophilic surface.

3. Numerical model materials and methods

Numerical models of the centrifugal PCR microchamber filling were developed using Computational Fluid Dynamics (CFD) techniques. More specifically, the Volume of Fluid (VOF) method was used to model the location of the fluid front (*viz.*, meniscus) during filling of the microchamber.[27] This work is a continuation of similar studies reported earlier in the literature by the Banerjee research group for numerical simulation and experimental validation using analytical models, numerical models (using the VOF method), and high-speed imaging experiments.[32,33,35]

In this study, microchamber filling for rotating reference frames (*i.e.*, centrifugal microfluidics) and inertial frames (*i.e.*, non-rotating) was analyzed using CFD-ACE+ computational software (ESI-CFD Corp., France-CFDRC). As a first step, the 3-D solid model used for machining, fabrication, and assembly of the μTAS CD was imported into the CFD workspace, the PCR microchamber geometry isolated, and the geometry then computationally discretized into volume elements (computational grids). The grid widths ranged from 5 microns to 50 microns, with a minimum skew angle of 60°. There were 7 layers of grids along the thickness of the microchamber, and the grid aspect ratios were limited to less than 5 to minimize numerical diffusion during the computations for the VOF solver. A total of 15 000 brick-type grids (voxels) were used in these simulations (see ESI†).

Table 1 Contact angle measurements for various surfaces involved in the PCR microchamber

Wall boundary surface	Contact angle
1A – Native polycarbonate	81.6°
1B – Plasma-treated polycarbonate: *Roof*	41.5°
2 – Adhesive (PSA): *Walls*	110.5°
3 – Adhesive metal foil: *Floor*	110.5°

The subsequent steps included defining the governing equations and establishing the initial and boundary conditions, discussed next. The simulations were then run using a PC with 2 GB of RAM and a 2 GHz processor; each simulation typically required 3 weeks of execution time.

Experimental observations showed that PCR microchamber filling occurred on a time scale of 0.1–1 s. Thus, simulations were performed in time steps ranging from $\sim 5 \times 10^{-7} - 10^{-8}$ s. Explicit formulations were used in solving the transient solutions, hence the Courant Fredrich Levy (CFL) condition was used and the CFL parameter set to 0.8. Such a low value of time steps and CFL criteria was imposed in order to obtain an appropriate sampling frequency in time to adequately capture the gravity oscillations (*i.e.*, to obtain the proper configuration of the "ripples" on the meniscus) and to ensure proper convergence of the numerical residuals for the pressure and velocity components. As a final step, the simulation results for the meniscus profile were compared to the experimental image data for corresponding non-dimensional time steps (defined below).

3.1 Governing equations

The coupled governing equations for the three-dimensional, transient, incompressible flow were solved after discretization of the geometry and application of the appropriate boundary and initial conditions. The fluids (water and air) were treated as incompressible Newtonian fluids, and temperature effects were neglected (since thermocycling was not performed in these experiments). Hence, the respective mass conservation (Continuity) and momentum conservation (Navier–Stokes) equations utilized to simulate 3–D flow in the PCR microchamber are reduced to:

$$\nabla \bullet \vec{v} = 0 \tag{2}$$

$$\rho \frac{\partial}{\partial t} \vec{v} + \rho \vec{v} \bullet \nabla \vec{v} = \vec{f} - \nabla p + \mu \nabla^2 \vec{v} \tag{3}$$

where ∇ is the spatial gradient operator, $\vec{v}$ is the three-dimensional velocity field, ρ is fluid density, t is time (absolute), $\bullet$ is the vector dot product, $\vec{f}$ is the body force acting on the fluid which can be a combination of gravity force components and inertial forces (*viz.*, Coriolis and centrifugal forces) due to rotation of the microchamber, p is pressure, and μ is kinematic viscosity. For the microchamber, the gravity force is very small (analytical estimates shows that the gravity forces are two orders of magnitude smaller than capillary and rotational forces), and thus neglected to save on computational costs.

The PCR microchamber consisted of water as the primary fluid and air as the secondary fluid. The interface between the two phases was tracked using the volume of fluids function (F) continuity equation for each phase as:

$$\frac{\partial F}{\partial t} + \vec{v} \bullet \nabla F = 0 \quad (4)$$

where F is the volume of fluids function ($F = 1$ in grids completely filled with water, $F = 0$ in grids filled with air, and F has a fractional value corresponding to the volume fraction of water in partially filled grids).[27] As discussed, DI water with a small amount of contrast agent was used as the test fluid, and so thermo-physical property values of water were used in the simulations. For air and water respectively (at room temperature, 25 °C), the density (ρ) is 1.614 kg/m^3 and 997 kg/m^3, the kinematic viscosity (μ) is 1.846×10^{-5} kg/m s and 8.55×10^{-4} kg/m s, and the surface tension (σ) of the air–water interface is 7.17×10^{-2} N/m.

3.2 Inlet, boundary, and initial conditions

The final steps prior to performing the numerical simulations were specification of the pressure conditions at the PCR microchamber inlet and outlet cross-sections, specification of the wall boundary conditions for the discretized model of the PCR microchamber to reflect the varying surface characteristics (*i.e.*, contact angles) for each surface, and the specification of initial conditions that assumed a certain volume of liquid in the inlet microchannel feeding the PCR microchamber. Following is a discussion and justification for the conditions chosen.

3.2.1 Inlet conditions. Numerical simulations were performed using several microchamber inlet pressures. The inlet pressure was adjusted to simulate the variation in rotationally-induced pressure at the entrance to the PCR microchamber from an appropriate length plug of fluid in the microchannel connecting the sample preparation fluidics to the PCR microchamber. Since the liquid column decreases in height as the microchamber is filled, the pressure at the inlet of the microchamber would be expected to decrease with time.

In the initial simulations, the inlet pressure was fixed at a range of gage pressures: 2 kPa, 1 kPa, and 0.5 kPa. These values were based on the pressure developed from the corresponding liquid column in the microchannel for a rotation speed of 2000 RPM, estimated as follows:

Due to rotation of a liquid column of finite length feeding the PCR microchamber, the centrifugal acceleration at each location will be proportional to the radial location and the square of the angular velocity. Hence, at any radius, $\bar{r}$, the linear acceleration, $\vec{a}$, is given as:

$$\vec{a} = \bar{r}\omega^2 \quad (5)$$

Using a control volume based analysis (for a closed system) for a microchannel of width w and depth h that is filled with liquid, the differential volume-of-liquid, $d\forall$, in a differential element, $d\bar{r}$, is given as:

$$d\forall = wh(d\bar{r}) \quad (6)$$

The differential pressure (dP) in the radial direction between the two control surfaces due to the volumetric forces acting on the fluid is given by:

$$dP = \rho\vec{a}(d\forall)/wh = \rho\omega^2\bar{r}d\bar{r} \quad (7)$$

Integrating this expression from eqn (7) for the extents of the liquid column (bounded between $\bar{r}_f$ and $\bar{r}_i$) yields the net gage pressure acting at the inlet of the microchamber, assuming the other end of the liquid column is at atmospheric pressure:

$$P = \rho\omega^2 \int_{\bar{r}_i}^{\bar{r}_f} \bar{r}d\bar{r} = \frac{1}{2}\rho\omega^2\left(\bar{r}_f^2 - \bar{r}_i^2\right) \quad (8)$$

Using the radial dimensions of the liquid column and the known rotation velocity, it is estimated that the inlet gage pressure is at 2 kPa at the beginning of the simulation, followed by a reduction of the inlet pressure as the height of the liquid column changes during the microchamber filling process. Based on this result, the calculated value of 2 kPa was chosen as an inlet pressure, as well as two lower values of 1 kPa and 0.5 kPa. It may be noted that in reality, this inlet pressure can be time-dependent due to the start-up transients/acceleration of the rotating control motor until steady-state rotation speeds are achieved.

Moreover, the inlet pressure can also change due to the continuous reduction of the liquid level in the connecting microchannel over time during depletion of liquid from the sample preparation fluidics. For the majority of microchamber filling time, the microchannel connecting the sample preparation fluidics and the PCR microchamber remains filled, and so the inlet pressure can be taken as a constant during this period. As the sample preparation fluidics begin to empty towards the end of the PCR microchamber filling cycle, the length of the liquid column in the microchannel decreases gradually until it fully empties. Thus, the PCR microchamber inlet pressure undergoes a corresponding decrease.

Hence, additional inlet conditions were simulated in which the inlet pressure begins at a constant value of 2 kPa, followed by a step decrease in the inlet pressure over the remaining 15–40% of microchamber filling duration (to be more consistent with the experimental observations). The step change in pressure can more accurately predict microchamber filling behavior without having to compromise significant additional computational execution time. The pressure was decreased from 2 kPa to constant values of 0.5 kPa and 1 kPa, each at two different points during filling, for a total of four different additional simulations. Description and justification for the two different pressure-step time points are detailed in a later section. For all varying inlet conditions, an outlet boundary condition at the exit of the PCR microchamber was specified to be at atmospheric pressure (*i.e.*, gage pressure of 0 Pa).

3.2.2 Boundary conditions. Next, the wall boundary conditions were specified. The boundary conditions used for the simulations involve wall boundary conditions (no-slip condition) with either hydrophobic or hydrophilic contact angles specified for each wall (to be consistent with the experimental conditions), as obtained from the contact angle measurements of the microchamber materials (Table 1). Fig. 3 shows a cross-section of the

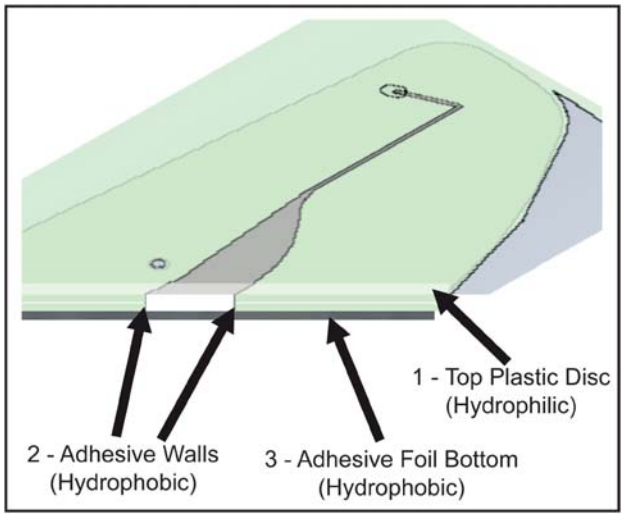

Fig. 3 Cross-section of the modeled PCR microchamber, showing the surface properties at each wall boundary condition. The contact angle values for the surfaces correspond to the values shown in Table 1.

PCR microchamber and the wall boundary conditions used with the contact angle specified for each surface. The contact angle of the fluid with the top surface (roof) is 41.5°. The upper, lower and bottom (floor) walls of the microchamber are hydrophobic, and the contact angle is 110.5°. All walls and surfaces were taken to be non-compliant and with static contact angles during the numerical simulations. In reality, the adhesive foil used to seal the PCR microchambers was found to be flexible and likely to deform during the filling process in response to pressure applied by the liquid. The walls were defined as rotating walls, with the axis of rotation at the CD center, and rotating at the same angular velocity as the global frame (2000 RPM).

3.2.3 Initial conditions. To start the simulation, initially it was assumed a small part of the microchamber inlet was filled with fluid. This allowed for the meniscus to form and stabilize quickly. Hence, a fluid-initial boundary condition was specified by imposing a fixed liquid volume (0.02% of the total microchamber volume) to exist at the inlet section of the PCR microchamber. This approximation was imposed to enable faster computation (*i.e.*, faster convergence of the simulation steps) without compromising accuracy of the predictions.

To match the simulation parameters with the experimental conditions, in the simulations the center of the rotational axis (corresponding to the center of the CD) was located at a distance 78 mm ($\bar{r}$ value) from the center of the microchamber (Fig. 1, inset). In the simulations, the uniform rotation speed was imposed at a steady-state value of 2000 RPM in the counter-clockwise direction to match the experiments. CD rotation was accounted for by performing the simulation in a global rotating frame of reference; the center of the rotation was set as the origin of the reference frame (0, 0, 0), and a constant angular rotation of (0, 0, 209.4) rad/s was applied to the global frame. It should be noted that in the experiments, a certain degree of variability is expected in rotation speeds as well as rotational acceleration during ramp-up of the CD. Additionally, a "control" simulation was run in a non-rotating reference frame at an inlet pressure condition of 2 kPa to serve as a reference against which the specific, centrifugally-induced behavior could be identified.

3.3 Data analysis and experimental validation

The experimental data (movie images obtained using the strobe-imaging system, described above) were compared with the numerical predictions. First, the movie files obtained from the high-speed imaging apparatus were digitized into individual frames. Edge detection routines using Matlab (MathWorks, Inc., MA, USA) were then used to demarcate the liquid region in the PCR microchamber. This was achieved by using appropriate threshold values for intensity in each image. This enabled the image intensity information to be set to a binary format with pixels representing the air phase being set to an intensity value of 1, and pixels in the darker liquid phase being set to 0. After edge detection, the number of pixels in the liquid phase was tabulated for each image obtained from the experiments. The fraction of microchamber filling (from experimental images) was obtained by taking the ratio of the number of liquid pixels of each frame (in time) with the number of liquid pixels when the microchamber is completely filled. In addition, time between frames (for experimental images) was calculated based on the 2000 RPM spin speed and the one-image-per-rotation condition, to obtain time stamps for each extracted frame. For the numerical results, the liquid volume fraction in the microchamber was calculated using numerical integration (*i.e.*, by counting the number of grids with a VOF function (F) value of 0.5 or higher).

4. Results and discussion

Validation of the numerical predictions with the experimental results was performed using both a quantitative method (*i.e.*, by plotting liquid volume fraction as a function of non-dimensional time) and a qualitative method (*i.e.*, by visually comparing the meniscus shape and position during filling). The liquid volume fraction (Φ) at any instant is defined as the ratio of volume of filled liquid present to the total, maximum volume of the PCR microchamber (*i.e.*, % filled, or, equivalently, a normalized filling value). The values of Φ are obtained from the experiments using image analysis described above. The VOF models were used to predict the location of the meniscus as a function of time, and subsequently used to calculate the value of Φ from the numerical values for F, as described above in eqn (4). The non-dimensional time (τ) is defined as the ratio of the actual time at any instant (t) to the total time (t_{max}) required to completely fill the microchamber at each condition (*i.e.*, % time, or, equivalently,

Table 2 Numerical simulations performed

Inlet pressure condition	Steady/dynamic	Comments
A: 2 kPa	Steady	—
B: 1 kPa	Steady	—
C: 0.5 kPa	Steady	—
D: 2 kPa → 1 kPa, τ_1	Dynamic	Step change at $\tau_1 = 0.6$
E: 2 kPa → 1 kPa, τ_2	Dynamic	Step change at $\tau_2 = 0.85$
F: 2 kPa → 0.5 kPa, τ_1	Dynamic	Step change at $\tau_1 = 0.6$
G: 2 kPa → 0.5 kPa, τ_2	Dynamic	Step change at $\tau_2 = 0.85$
H: 2 kPa	Steady	Non-rotating

a normalized filling time). In this section, the quantitative results are discussed first. A best-match simulation condition is identified, and this single condition is then focused on in the following qualitative discussion. As a guide during this section, Table 2 lists all conditions simulated using the numerical methods.

4.1 Microchamber filling: volume fraction calculations

4.1.1 Pressure results. Fig. 4 shows the comparison of experimental and simulation images for a single numerical simulation. Fig. 5 shows results from the 8 numerical simulations performed (Table 2), including all rotating reference frame simulations performed at varying PCR microchamber inlet pressures as well as the non-rotating reference frame simulation. These results are compared with the experimental data, also shown in Fig. 5, for filling behavior. Fig. 6 shows the absolute total filling time (t_{max}) for the different simulation predictions and experimental result.

As discussed, the filling behavior is presented by plotting the liquid volume fraction (Φ) as a function of non-dimensional time (τ) in Fig. 5. The experimental data show a marked oscillation in the flow rate that develops during the initial stages of the filling. These oscillations are found to increase with the progression of microchamber filling. These strong oscillations are not observed in the numerical predictions, but are explained by several factors. First, the top-bounding wall of the PCR microchamber is made of a thin layer of adhesive that can be expected to exhibit flexibility. During the filling process, the dynamic pressure and shear forces induced on the flexible wall can lead to fluid-structure interactions causing bulging of the chamber wall; such fluid-structure interactions can result in the observed oscillations in filling rate. In addition, the decreasing length of the liquid column feeding the PCR microchamber inlet can cause variations in pressure leading to coupled modes of oscillation in the fluid column. Finally, a slight offset between the control motor axis-of-rotation and the CD center could give rise to such filling rate oscillations.

As shown in Fig. 5, the filling behavior predicted by the numerical simulations is observed to be sensitive to the inlet pressure condition. As an example, the predictions for filling behavior at the 1 kPa steady inlet pressure condition (condition B) deviates sharply from the experimental data. The slope for the filling behavior at the 1 kPa inlet pressure distinctly transitions from a slower to a faster rate at a point corresponding to $\tau \sim 0.65$ and $\Phi \sim 0.5$. A distinct change in filling rate (change in slope) is also observed at $\tau \sim 0.9$ and $\Phi \sim 0.8$. In the final stages of filling, the slope is drastically reduced to almost 0 (or a very small filling rate) at $\tau > 0.99$ and $\Phi > 0.99$. At the simulation times corresponding to the increase in slope, a distinct oscillation (or traveling wave pattern) is observed on the meniscus shape during the

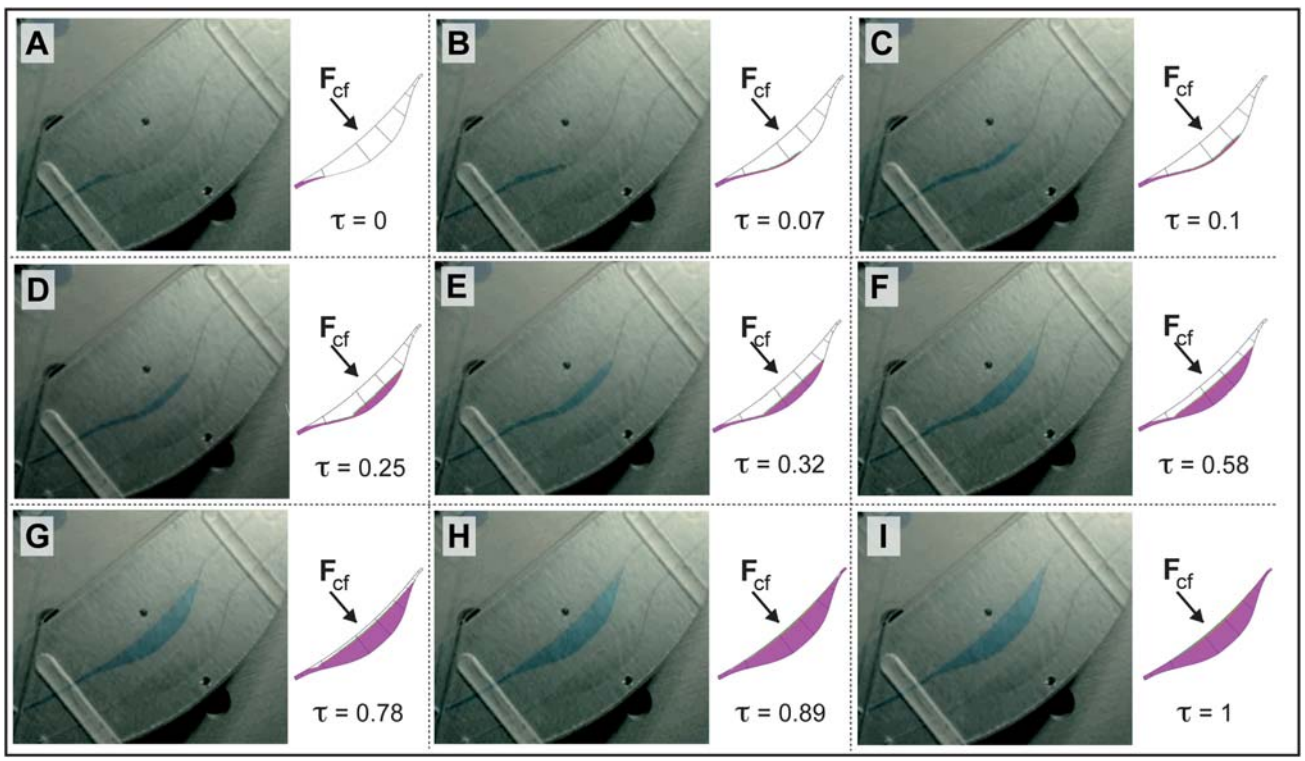

Fig. 4 Comparison of numerical simulation predictions (right) performed with a rotating reference frame (2000 RPM) at a dynamic inlet pressure condition step-changing from 2 kPa to 0.5 kPa at $\tau = 0.6$ with experimental images (left) for filling of a PCR microchamber on the μTAS CD. Arrow indicates direction of centrifugal force and τ represents the non-dimensional filling time constant (t/t_{max}). (A) Chamber begins filling from the left ($\tau = 0$), (B) Fluid is pushed towards the lower contour of the chamber due to centrifugal force as filling continues ($\tau = 0.07$), (C) Nearly the entire bottom of the chamber wall is in contact with fluid ($\tau = 0.1$), (D) The chamber begins filling from the "bottom-up" ($\tau = 0.25$), (E) Retrograde flow is present as some fluid travels against the bulk flow movement, causing mixing in of air ($\tau = 0.32$), (F) Filling continues ($\tau = 0.58$), (G) Chamber is nearly full ($\tau = 0.78$), (H) Only a small channel of air exists on the top of the chamber as the outlet port begins to fill, non-linear interactions appear, and further retrograde flow is present ($\tau = 0.89$), (I) Filling is complete, with the chamber and outlet port uniformly filled with liquid ($\tau = 1$).

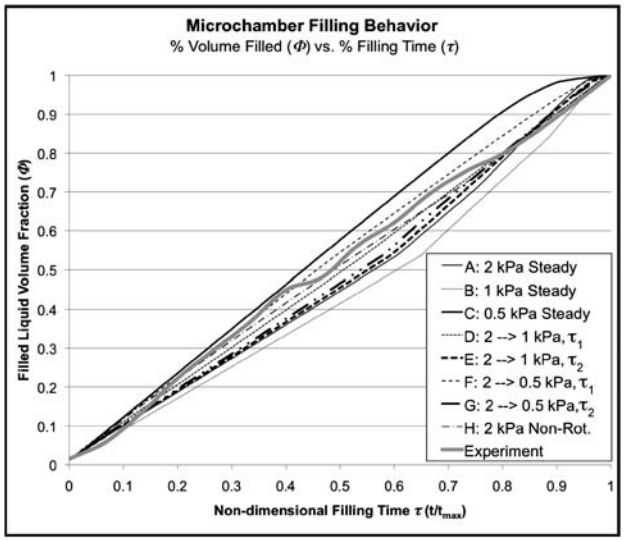

Fig. 5 Comparison of numerical predictions with experimental data for liquid volume fraction (Φ) as a function of non-dimensional time (τ). Plots shows that numerical simulation F provides the best match to the experimental data.

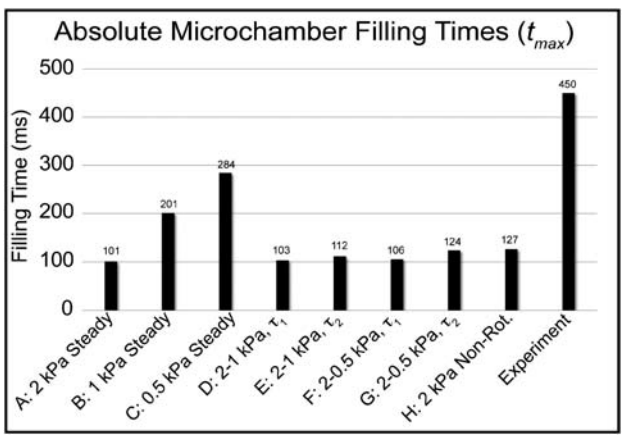

Fig. 6 Numerical predictions and experimental results for total microchamber filling time (t_{max}).

filling of the microchambers (as described above). This meniscus oscillation results in higher capillary forces (longer contact line length) resulting in a higher filling rate. During the final stages of filling, the meniscus oscillation is found to cause re-attachment and quasi-periodic separation of the meniscus from the upper wall; this leads to a higher frictional drag (due to an increase in the effective wetted perimeter and a reduction in the effective hydraulic radius). A smaller hydraulic radius causes a higher frictional pressure drop and thus a reduction in the flow rate, leading to drastic reduction in filling rate.

Sensitivity of the numerical simulations to the inlet pressure can also be observed by examining the steady 0.5 kPa inlet pressure condition (condition C). This condition also shows deviation from the experimental results. The trends in the slope for the filling rate are similar to those observed for the 1 kPa inlet pressure, though the deviation is comparatively higher (Fig. 5). Also, lower rates of filling are observed, as would be expected for a lower pressure. The slope for the filling behavior at the 0.5 kPa inlet pressure is nearly constant, except during the final stages of the filling where the filling rate is very small. This reduction in filling rate occurs at a later time (as compared to the 1 kPa case) due to slower filling of the PCR microchamber; therefore, reattachment/separation of the meniscus profile with the upper wall occurs at a later stage. This results in a drop in filling rate and therefore a significantly higher time for filling the chamber (Fig. 6).

Simulation results for the steady 2 kPa inlet pressure condition (condition A) show trends in the slope for the filling rate are similar to those observed for the 1 kPa inlet pressure, though deviation from the experimental result is comparatively lower. Also, higher rates of filling are observed, as would be expected for a higher pressure. The slope for the filling behavior at the 2 kPa inlet pressure distinctly transitions from a slow rate to a faster rate at a point corresponding to $\tau \sim 0.6$ and $\Phi \sim 0.5$. A marginal change in filling rate is also observed at $\tau \sim 0.7$ and $\Phi \sim 0.7$. Similar to the above 0.5 and 1 kPa cases, in the final stages of filling the slope is drastically reduced to almost 0 (or a very small filling rate) at $\tau > 0.97$ and $\Phi > 0.97$. This reduction in filling rate occurs at an earlier time (as compared to the 1 kPa case) due to faster filling of the chamber. This results in a drop in filling rate at a comparatively earlier time.

Hence, the additional simulations performed by changing the inlet pressure condition by a step change from 2 kPa $\rightarrow$ 1 kPa and 0.5 kPa are expected to be a more accurate reflection of the experimental conditions. This is due to the microchannel connection between the sample preparation fluidics and PCR microchamber inlet being filled during the majority of microchamber filling, but then emptying late in the microchamber filling sequence, as discussed above.

From the simulations, it was observed that the steady 2 kPa predictions for the filling rate intersect the experimental results at $\tau \sim 0.85$. Also, the filling rate is found to start drastically accelerating at $\tau \sim 0.6$. These observations from the initial 2 kPa simulation were used to determine at what time the pressure steps should occur for the dynamic 2 $\rightarrow$ 0.5 kPa and 2 $\rightarrow$ 1 kPa simulation conditions. Thus, the step changes were performed at two different τ values of 0.6 (τ_1) and 0.85 (τ_2). It is observed that the step change in inlet pressure boundary condition results in a far better fit with the experimental data.

The inlet pressure simulation condition that changes from 2 kPa $\rightarrow$ 0.5 kPa at $\tau_1 = 0.6$ (condition F) provides a very accurate match of filling behavior to the experimental data, with an R^2 value of over 0.99. Indeed, Fig. 4 and 5 show that this match is excellent, and represents an extremely accurate model for filling behavior of the PCR microchamber.

The resolution on the frame rate of the experimental images (one image per rotation) did not enable fine-detail observation of the reduction in flow rates as observed in the numerical predictions. Also, surprisingly, the predictions for the non-rotating reference frame (which showed poor match for the meniscus profiles), showed a good match with the filling rate behavior for experiments, especially in the final stages of filling. However, the match of the meniscus profile was poor (discussed further below). Pressure drop characteristics due to the balance between viscous forces and capillary forces dominate the fluid flow behavior when the microchamber is filled almost completely, and the centrifugal

forces possibly are not as dominant at this stage. Hence, a linear profile in chamber filling is observed in the final stages, which matches well with the non-rotating case simulation results.

4.1.2 Filling time results. Fig. 6 shows the absolute time taken to fill the PCR microchamber for the various conditions, including the experimental data. The results show that the time for microchamber filling is strongly dependent on the inlet pressure conditions. A higher inlet pressure causes higher flow rates, and therefore lower filling time. The hydrodynamic flow resistance of the inlet and outlet channels (including those of the sample preparation fluidics feeding the PCR microchamber) is a contributor to a longer filling time. Moreover, the results show that the microchamber filling time is significantly larger (2× more) for the experimental data than for the numerical predictions; this is likely caused by 3 aspects of the system not taken into account during the numerical modeling.

The first, and likely the most significant, is that the thin metal foil used for the bottom of the PCR microchamber is compliant, even though the numerical models considered this surface non-compliant (as discussed above). As the CD spins at the relatively high speed of 2000 RPM, the metal foil bulges, causing an increased fill time and a slightly increased volume. Another aspect of the system not taken into account is the outlet pressure. The μTAS CD involves a self-venting mechanism; the system is closed to the outside environment, and air cycles through the system to replace fluid as it moves. Thus, the pressure at the microchamber outlet port may have been slightly higher than the atmospheric pressure modeled, slowing microchamber filling. Finally, there are inevitable surface-roughness anomalies created during the CD fabrication process. The adhesives used to make the PCR microchamber do not get cut perfectly clean at the edges, and this roughness may have contributed further to a slightly longer filling time. However, the numerically simulated filling time is on the same order as the experimental filling time (on the order of 100s of ms). In reality, these variations observed have little practical impact on CD operation and use. The more important characteristic of filling behavior has been modeled accurately, and can thus be used to guide microchamber design to obtain complete, uniform filling.

4.2 Microchamber filling: visualization results

The previous quantitative section showed that the simulation performed under the inlet-pressure condition of 2 kPa → 0.5 kPa with the step change at $\tau_I = 0.6$ (condition F from Table 2) provided the best fit with the experimental data. Thus, this condition is focused on here for a qualitative discussion of microchamber filling. Fig. 4 shows a sequence of images for the meniscus position in the PCR microchamber obtained from the flow visualization experiments compared to the numerical prediction for the meniscus location obtained from the best-match VOF simulation.

Qualitatively, an excellent match is observed for the shape of the meniscus and the location of the meniscus between the numerical prediction and the experimental data. Image data from both the experiments and numerical prediction show that the meniscus is pushed to the lower wall by the centrifugal forces during the initial stages of filling (*e.g.*, Fig. 4C). As a result, the microchamber is supplied with liquid from the inlet, and the microchamber fills partially from the lower wall upwards (towards the CD center). As the liquid level builds from the lower wall towards the upper wall, the liquid meniscus approaches the microchamber outlet before it establishes complete contact with the upper wall (Fig. 4H). As a result, a complex, non-linear interaction between the inlet and outlet sections of the microchamber occurs. This gives rise to oscillations in the meniscus, which unexpectedly alters the filling rate during various stages.

Another unexpected and complex display of fluidic behavior observed during filling is due to the aforementioned meniscus oscillations. The meniscus is observed to have a reversal in flow direction when the non-linear interaction between inlet and outlet sections of the microchamber occurs (Fig. 4H). This results in the meniscus moving backwards from the outlet section towards the inlet section when the microchamber is partially filled. Moreover, retrograde flow is observed midway during filling (Fig. 4D–G). The bulk fluid in the microchamber is seen to establish a secondary meniscus that moves in the opposite direction of bulk fluid flow. Both of these retrograde flow observations are unexpected, and, with a different microchamber geometry, would likely be hindrances to uniform filling. However, the observed flow reversal patterns may beneficially enhance meniscus driven mixing within the liquid. This could be useful, for example, if mixing is needed to reconstitute buffers or reagents that have been loaded or lyophilized inside the PCR microchamber.

An additional simulation was performed for filling of the microchamber at no rotation (inertial reference frame). This study served as a control, and was performed to explore the differences in flow behavior in the presence and absence of centrifugal forces during the filling. Fig. 7 shows the results from the no-rotation case of the meniscus position as a function of time compared with the corresponding results for filling at 2000 RPM (both simulations were performed for a fixed, 2 kPa inlet

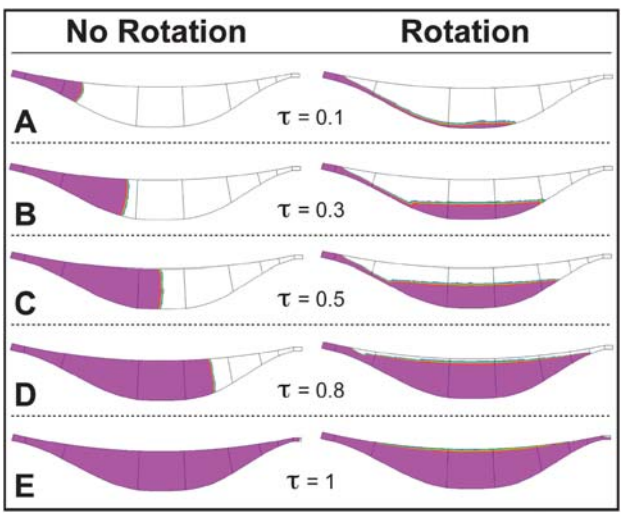

Fig. 7 Comparison of chamber filling without rotation and with rotation at 2000 RPM for varying τ values; both inlet pressures were set at a steady 2 kPa.

pressure condition). In the no-rotation case, it is observed that the fluid flow spans the full cross-section of the microchamber and proceeds with a uniform filling rate as a function of time, as expected for a solely pressure-driven system. In contrast, the flow behavior with rotation is distinctly different (as observed experimentally and numerically), as discussed above. Thus, the majority of the complex fluidic behavior observed is a result of the contributions from the rotationally-induced centrifugal and Coriolis forces.

4.3 Practical applications for microchamber design

The model developed here can be generalized and extrapolated for use as a guide for microchamber geometry design, and to better understand both channel/chamber filling and emptying on centrifugal platforms. Moreover, the model can be used to characterize non-centrifugal, pressure-driven systems by performing simulations under no-rotation conditions. Once the appropriate surface properties (*i.e.*, contact angles), geometries, pressure conditions, and, in the case of a CD system, rotation speeds, are identified, these practical characteristics can be used as inputs to the VOF model. This allows modeling and prediction of the varying surface properties and resulting complex surface interactions along with the multifaceted force components involved in microfluidic platforms that can result in unexpected behavior. This is particularly burdensome when trying to design microchambers where complete, uniform liquid filling is required, as discussed. However, the work presented here has shown that the model developed can be used in a practical manner during CD design and testing. It should also be mentioned that the microchamber utilized here was designed taking into account that the force lines on centrifugal platforms are in a polar coordinate system, not a linear system. Thus, the contours of the microchamber follow the contours of the centrifugal force lines, ensuring uniformity in the resultant force fields and thus obviating any hindrance to fluid flow for uniform chamber filling. With an accurate, adaptable model to drive a well-guided design methodology, uniform, bubble-free filling of microchambers on centrifugal platforms can be achieved along with an in-depth understanding of the complex, coupled, and non-linear interactions in the constitutive force fields present in the system. The force fields can modify the fluid behavior drastically even with small changes in the experimental, geometric, and operational parameters.

5. Conclusions

Numerical modeling using the Volume of Fluids method was utilized to study the complex microchamber filling behavior in a novel centrifugal microfluidic platform. The numerical model predictions were compared with the experimental results by both a qualitative method (by visually comparing the meniscus shape and position during filling) and a quantitative method (by plotting filled liquid volume fraction as a function of non-dimensional time). The meniscus shape and position visual comparison was found to have a good qualitative match, revealing unexpected complex filling behavior (*i.e.*, retrograde flow oscillations). For the input pressure condition of a step change from 2 kPa $\rightarrow$ 0.5 kPa at a τ of 0.6, the numerical predictions were found to have 99% agreement with the experimental channel filling profiles.

Future research activities will complement current fluidic models with thermal modeling of heating/cooling elements on the CD for such tasks as DNA amplification (*e.g.*, PCR) and phase change-based valves (*e.g.*, ice-valves with thermoelectric coolers/heaters). Such an analysis, coupled with experimental validation, is essential for realization and implementation of a wide range of clinical sample-to-answer systems utilizing centrifugal microfluidics.

Acknowledgements

The authors wish to thank the DARPA MF3 center for funding of the presented research, and Dr Horacio Kido for assistance during CD fabrication and PCR microchamber design. The authors also wish to acknowledge the support by ESI-CFD in providing the modeling tools (CFD-ACE+) and technical support for the software.

Notes and references

1 M. Madou, *Fundamentals of Microfabrication*, 2nd edn, CRC Press, Boca Raton, London, New York, and Washington D.C., 2002.
2 A. Manz, N. Graber and H. Widmer, *Sens. Actuators, B*, 1990, **1**, 244–248.
3 D. Erickson and D. Li, *Anal. Chim. Acta*, 2004, **507**, 11–26.
4 G. Fiorini and D. Chiu, *BioTechniques*, 2005, **38**, 429–446.
5 H. Becker and C. Gartner, *Electrophoresis*, 2000, **21**, 12–26.
6 D. Duffy, J. McDonald, O. Schueller and G. Whitesides, *Anal. Chem.*, 1998, **70**, 4974–4984.
7 Z. Nie and E. Kumacheva, *Nat. Mater.*, 2008, **7**, 277–290.
8 L. Hung, R. Lin and A. Lee, *Lab Chip*, 2008, **8**, 983–987.
9 J. Castillo, M. Dimaki and W. Svendsen, *Integr. Biol.*, 2009, **1**, 30–42.
10 A. Kamholz, B. Weigl, B. Finlayson and P. Yager, *Anal. Chem.*, 1999, **71**, 5340–5347.
11 J. Liu and M. Lee, *Electrophoresis*, 2006, **27**, 3533–3546.
12 H. Craighead, *Nature*, 2006, **442**, 387–393.
13 J. Wang, *Talanta*, 2002, **56**, 223–231.
14 J. West, M. Becker, S. Tombrink and A. Manz, *Anal. Chem.*, 2008, **80**, 4403–4419.
15 D. Duffy, H. Gills, J. Lin, N. Sheppard and G. Kellogg, *Anal. Chem.*, 1999, **71**, 4669–4678.
16 M. Madou, J. Zoval, G. Jia, H. Kido, J. Kim and N. Kim, *Annu. Rev. Biomed. Eng.*, 2006, **8**, 601–628.
17 J. Steigert, T. Brenner, M. Grumann, L. Riegger, S. Lutz, R. Zengerle and J. Ducrée, *Biomed. Microdevices*, 2007, **9**, 675–679.
18 M. Madou, L. Lee, S. Daunert, S. Lai and C. Shih, *Biomed. Microdevices*, 2001, **3**, 245–254.
19 G. Whitesides, *Nature*, 2006, **442**, 368–373.
20 G. Kovacs, *Micromachined Transducers Sourcebook*, McGraw-Hill, New York, 1998.
21 M. Pollack, A. Shenderov and R. Fair, *Lab Chip*, 2002, **2**, 96–101.
22 J. Zeng, D. Banerjee, M. Deshpande, J. Gilbert, D. Duffy and G. Kellog, *Proc. in MicroTAS*, 2000, Amsterdam.
23 T. Brenner, T. Glatzel, R. Zengerle and J. Ducrée, *Lab Chip*, 2005, **5**, 146–150.
24 J. Ducrée, T. Brenner, S. Haeberle, T. Glatzel and R. Zengerle, *Microfluid. Nanofluid.*, 2006, **2**, 78–84.
25 J. Ducrée, S. Haeberle, T. Brenner, T. Glatzel and R. Zengerle, *Microfluid. Nanofluid.*, 2006, **2**, 97–105.
26 D. Kim and T. Kwon, *Microfluid. Nanofluid.*, 2006, **2**, 125–140.
27 C. Hirt and B. Nichols, *J. Comput. Phys.*, 1981, **39**, 201–225.
28 G. Jia, K. Ma, J. Kim, J. Zoval, R. Peytavi, M. Bergeron and M. Madou, *Sens. Actuators, B*, 2006, **114**, 173–181.

29 G. Jia, J. Siegrist, C. Deng, J. Zoval, G. Stewart, R. Peytavi, A. Huletsky, M. Bergeron and M. Madou, *Colloids Surf., B*, 2007, **58**, 52–60.
30 H. Kido, M. Micic, D. Smith, J. Zoval, J. Norton and M. Madou, *Colloids Surf., B*, 2007, **58**, 44–51.
31 H. Tsai, E. Moschou, S. Daunert, M. Madou and L. Kulinsky, *Adv. Mater.*, 2009, **21**, 656–660.
32 D. Banerjee, N. Amro, S. Disawal and J. Fragala, *J. Microlithogr., Microfabr., Microsyst.*, 2005, **4**, 023014–023021-8.
33 D. Banerjee, *Proc. in Nano Science and Technology Institute (NSTI) Nanotechnology 2005|NanoBio2005*, 2005, Anaheim, CA, USA.
34 A. Larsson and H. Dérand, *J. Colloid Interface Sci.*, 2002, **246**, 214–221.
35 D. Banerjee, *Proc. in INTERPACK2005, The ASME|Pacific Rim Technical Conference and Exhibition on Integration and Packaging of MEMS, NEMS and Electronic Systems*, 2005, San Francisco, CA, USA.

